

Modeling and sea trial of a self-powered ocean buoy harvesting Arctic Ocean wave energy using a double-side cylindrical triboelectric nanogenerator

Hyunjun Jung^a, Zhaocheng Lu^a, Wonseop Hwang^a, Brianna Friedman^a, Andrea Copping^a, Ruth Branch^a, Z. Daniel Deng^{a,b,*}

^a Energy and Environment Directorate, Pacific Northwest National Laboratory, Richland, WA 99354, USA

^b Department of Naval Architecture and Marine Engineering, University of Michigan, Ann Arbor, MI 48109, USA

ARTICLE INFO

Keywords:

Arctic Ocean
Buoy motion modeling
Cylindrical triboelectric nanogenerator
Wave energy
Frequency-multiplying
Ocean observation system

ABSTRACT

Maximizing the output power of a triboelectric nanogenerator (TENG) system for ocean buoy applications requires an understanding of the effects of sea states and wave conditions on buoy motion. Previous studies have explored the hydrodynamics of buoys for wave energy harvesting using TENGs, but they often relied on simplified models that used a single wave period and pitch amplitude, which may not fully capture the complexity of real-world sea conditions. In this study, we present a numerical simulation model of Arctic-TENG buoy dynamics to predict and optimize its mechanical behavior in the Arctic Ocean. First, a local sea trial was conducted to collect empirical data on sea states and buoy motion. The data were used to validate the buoy simulation model, which agreed well with the sea trial results, with differences of 13.6 % and 13.2 % in root mean square angular displacement and angular velocity of buoy motion, respectively. The verified model was then used to predict buoy motion in the Arctic Ocean and to optimize the buoy design for greater angular amplitude and velocity, thereby enhancing TENG performance. These optimizations were experimentally validated using a custom buoy motion simulator: the maximum average power output of 2.28 mW was observed at a 20 MΩ load, and the instantaneous power output at this optimal load was recorded, showing that the majority of peak power ranged between 10 mW and 20 mW, with the maximum peak power output reaching 22 mW. This power level is sufficient to support satellite communications exceeding 500 bytes daily in ocean buoys. This work not only improved the TENG power output but also provided a comprehensive design guideline for energy harvesters in remote and harsh environments like the Arctic Ocean.

1. Introduction

Monitoring the Arctic Ocean is critically important for understanding and predicting changes in Arctic conditions, which have profound effects on the global climate [1,2]. Ocean observation systems, such as those deployed on buoys, play a crucial role in this effort by providing real-time data on sea ice dynamics, temperature, salinity, and other vital parameters [3,4]. However, the operational lifespan of these systems is typically limited to a few months [5], and their frequent deployment contributes to environmental pollution. One of the key challenges in maintaining these systems is providing a reliable and sustainable power supply, especially in the harsh and remote environment of the Arctic Ocean [6]. Renewable energy sources, particularly ocean wave energy,

offer a promising solution for powering these observation systems [7]. Unlike harvestable solar and wind energy at high latitudes, wave energy remains available when other sources are not.

Triboelectric nanogenerators (TENGs) have emerged as a cutting-edge technology for harvesting ocean wave energy, presenting a viable solution for powering ocean buoys. Additionally, TENGs are lightweight and offer high power density, enabling a more compact system design. Moreover, the primary TENG material, fluorinated ethylene propylene (FEP), is eco-friendly [8], further contributing to environmental sustainability. Since their introduction in 2014 [9,10], TENGs have been extensively explored for their ability to convert mechanical energy from waves into electrical energy. Their designs and applications have evolved, with several studies demonstrating their

* Corresponding author at: Energy and Environment Directorate, Pacific Northwest National Laboratory, Richland, WA 99354, USA.

E-mail address: Zhiquan.deng@pnnl.gov (Z.D. Deng).

<https://doi.org/10.1016/j.nanoen.2024.110641>

Received 12 November 2024; Received in revised form 15 December 2024; Accepted 31 December 2024

Available online 2 January 2025

2211-2855/© 2025 Battelle Memorial Institute.

Published by Elsevier Ltd.

This is an open access article under the CC BY license

(<http://creativecommons.org/licenses/by/4.0/>).

effectiveness in real-world conditions. For instance, Rodrigues et al. [11] developed a TENG-based buoy using an integrated rolling-sphere mechanism, achieving an output power of 230 μW under controlled wave conditions. In 2023, Wang et al. [12] reported a stacked disc-type rolling TENG (SDR-TENG) for ocean buoys, capable of generating 7.6 mW under wave conditions of 0.8 Hz. More recently, Zhang et al. [13] developed hybrid-type (triboelectric-electromagnetic) nanogenerators for self-powered buoys, showing high power densities (i.e., 141.7 W/m^3 for the TENG and 400 W/m^3 for the electromagnetic generator) under a wave frequency and a height of 0.83 Hz and 0.25 m, respectively, showing their potential to power a marine environmental monitoring network. TENGs are particularly well suited for deployment in the Arctic because of their enhanced performance at low temperatures [14–16]. Our previous work introduced the frequency-multiplied cylindrical TENG (Arctic-TENG), which is designed specifically for Arctic conditions [17,18]. The Arctic-TENG demonstrated superior performance at low temperatures, as low as -40°C , achieving a peak power density of 21.4 W/m^3 at 0.2 Hz in a controlled out-of-water wave simulator [18].

Double-sided cylindrical TENGs have proven to be effective for improving the power density of TENG devices [19–22]. Zhao et al. designed a wave energy converter incorporating a multilayered soft-brush cylindrical triboelectric nanogenerator with an electromagnetic generator (hybrid system). In the water tank test, it generated 2600 V rectified peak open-circuit voltage and 78 μA peak rectified short-circuit current under 0.8 Hz, which was enough to light up over 10,080 LEDs [19]. Han et al. designed a double-sided fluff and double Halbach array-structured hybrid triboelectric-electromagnetic nanogenerator (FH-HG) for harvesting ultra-low frequency wave energy, and the peak power of the TENG reached 2.02 W/m^3 under excitation at 1.4 Hz [20]. However, these double-sided cylindrical TENGs are more suitable for deployment on stable structures such as fixed offshore platforms or along the coastline. To develop a double-sided cylindrical TENG suitable for deployment on a free-floating platform, a fully integrated double-sided cylindrical TENG system specifically designed for a free-floating ocean buoy is needed.

To further enhance the output power of TENGs in buoys, it is essential to investigate the effect of the sea states and wave conditions on the buoy and to optimize the corresponding motions of the buoy, as the TENG's performance is directly influenced by the buoy dynamics. Researchers have recognized the influence of wave characteristics on the TENG power output. Using wave basin tests, Rodrigues et al. [11] clearly showed that electrical output depends significantly on the pitch degree of freedom, highlighting the importance of considering the full buoy dynamics, not just the TENGs, when subjected to wave excitations. Gonçalves et al. [23] optimized the dynamics of the buoy to effectively tune design parameters, thereby enhancing TENG output and making it better suited for specific sea states. Typically, each analytical cycle uses only one representative pair of wave period and pitch amplitude. Although multiple combinations could provide a more comprehensive analysis, more representative wave conditions reflecting real and complex sea states are needed for accurate TENG analysis and optimization.

In this study, we developed a numerical simulation model of Arctic-TENG buoy dynamics to predict and optimize the generator's mechanical motion under Arctic Ocean conditions. We began with a sea trial in the Salish Sea, which represents the inland seas of Puget Sound and Georgia Basin, connected to the Northeast Pacific Ocean by the Straits of Juan de Fuca. This trial provided essential data on sea states and buoy motion. The data were used to construct and validate our simulation model. Using the verified model, we optimized the physical parameters of the Arctic-TENG buoy to maximize its swing motion amplitude and speed in Arctic Ocean conditions. Additionally, we developed a two-degrees-of-freedom custom desktop buoy motion simulator to replicate the buoy's motion under Arctic Ocean conditions. To estimate the relevant energy power output, we integrated buoy dynamics simulation results with experimental testing of the TENG using the custom desktop

buoy motion simulator. The Arctic-TENG design was also enhanced by adding a second inner stator and modifying the rotor to a double-sided configuration, resulting in an increased power density of 34.6 W/m^3 . This study not only provides a solution for improving TENG power density but also offers guidelines for designing energy harvesters for deployment in inaccessible regions like the Arctic Ocean.

2. Results and discussion

2.1. Device structure and working principle

The frequency-multiplied cylindrical TENG (FMC-TENG) was chosen for the Arctic Ocean application because it is optimized for low-frequency wave applications [17]. The FMC-TENG is a freestanding, soft-contact TENG that converts wave energy into electricity. To further improve the energy density for the Arctic Ocean TENG (AO-TENG), the rotor was reconfigured to be double-sided with inner and outer stators. Fig. 1a shows the AO-TENG. The negatively charged material, fluorinated ethylene propylene (FEP), shown in green, is located on the rotor, whereas the positively charged material (aluminum) in red and yellow, and the soft-contact material (fur) in brown are located on the stators. Fig. 1b and c are photographs of the disassembled AO-TENG (Fig. 1b) and assembled AO-TENG (Fig. 1c). Consequently, the AO-TENG contains two sets of TENG units: the outer TENG, comprising the external stator and the outer side of the rotor, and the inner TENG, made up of the internal stator and the inner side of the rotor (Fig. 1b). The relevant schematic demonstrating the electrostatic induction process of the double-sided TENG energy harvesting system is in Fig. S1 and Note S1.

In our previous work [18], we optimized the TENG system to efficiently generate power under low-temperature conditions. This optimization was validated through durability experiments spanning over 3 million cycles. To ensure reliable functionality in Arctic environments, we further incorporated these optimized components [18] into the AO-TENG system, such as by applying low-temperature grease to the gear and low-friction bearing system. Typically, a buoy hull contains the AO-TENGs and swings as it encounters incoming ocean waves. Therefore, the buoy hull converts the wave motion into its swinging motion, and the swinging motion causes the rotors of the AO-TENG to spin for energy harvesting. Fig. 1d shows an example of the AO-TENG harvesting wave energy.

If a one-directional wave coming from the right is propagating to the left, the AO-TENG in the buoy starts at the trough of the wave (Fig. 1d, State i) such that the magnet attached to the bottom of the rotor is repelled from the magnet attached to the bottom of the stator, and the rotor sits off-center from the stator. As the AO-TENG continues to ride the wave (Fig. 1d, State ii) the entire unit slightly rotates to stay perpendicular to the wave (see the grey dashed line during State ii, Fig. 1d). Eventually the AO-TENG rotates more, and the rotor enters the “breaking point” (Fig. 1d, State iii) where the weight in the rotor overcomes the repelling force of the magnets (because of the increase in angle α), triggering a sudden swing motion of the mass that increases the angular velocity of the rotor, enhancing the output power of the TENG system. As the AO-TENG passes the crest and moves downward to the wave trough, another triggering event occurs (Fig. 1d, State iv), generating electricity. The sequence from State i to State iv repeats with each wave cycle.

An in-air, single-degree-of-freedom (SDOF) oscillator (Fig. 2a) was used to test the AO-TENG under simulated angular motions of the platform (e.g., a buoy). This oscillator is a slider-crank system with the crank driven by a DC motor and the slider constrained by a vertical rail. Simultaneously, another slider attached to the connecting rod is also sliding in another rail integrated on the oscillator platform, which functions as a rocker and used for installing the AO-TENG (Fig. 2a). Consequently, the simulator platform can oscillate $\pm 60^\circ$. The AO-TENG was tested at 0.2 Hz, which is the average wave frequency experienced in our location of interest in the Arctic Ocean [18]. The electrical

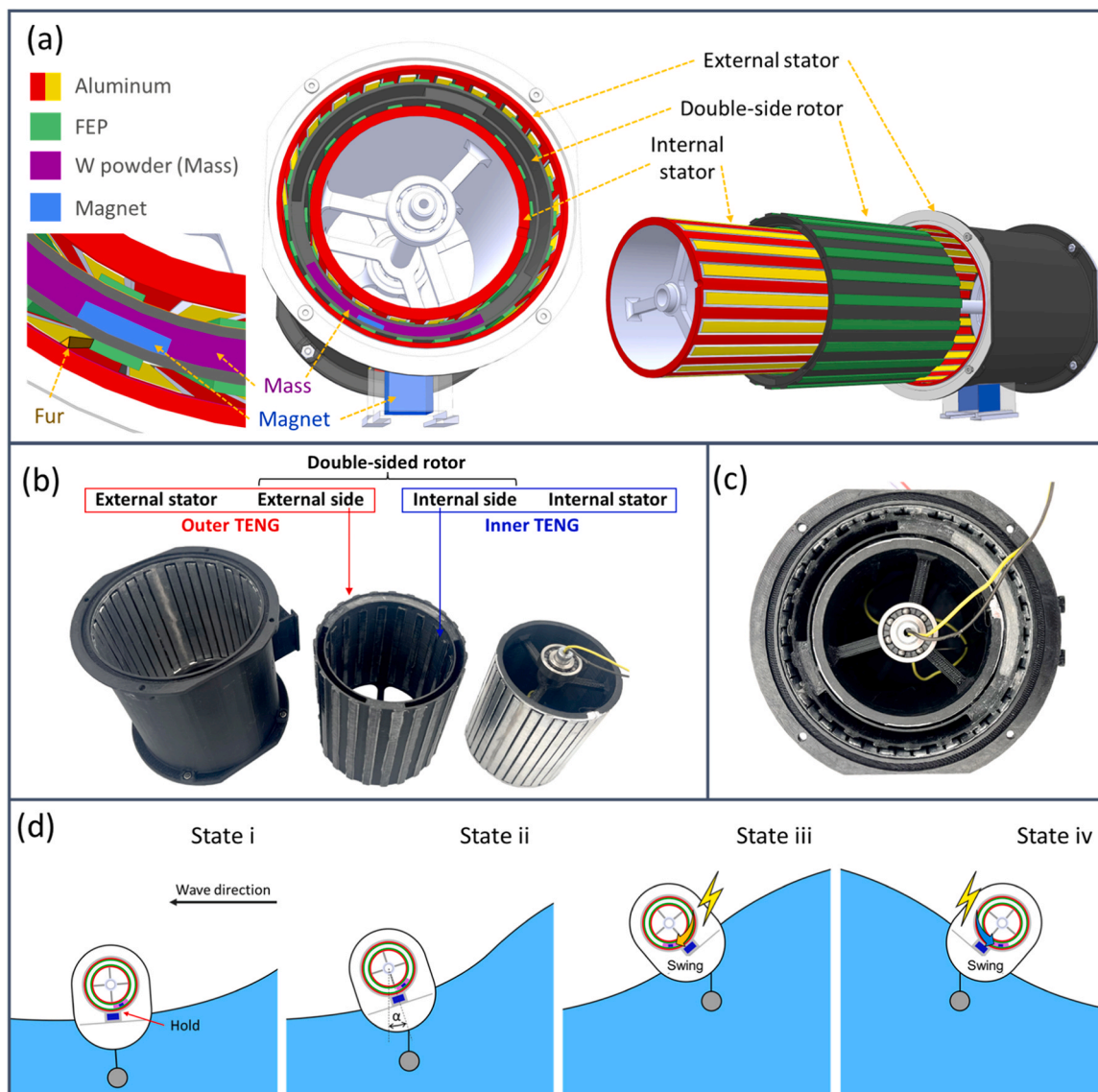


Fig. 1. Device structure and working mechanism of the AO-TENG. (a) Schematic of the AO-TENG and its materials. (b) Photograph of the external stator (left), double-sided rotor (middle), and internal stator (right) of the AO-TENG, and definition of inner and outer TENGs. (c) Photograph of a fully assembled AO-TENG. (d) Illustration of the wave-energy-to-electricity conversion of an AO-TENG integrated into a buoy hull encountering an ocean wave.

characteristics of the AO-TENG were measured. The open-circuit voltage (V_{oc}), short-circuit current (I_{sc}), and the transferred charge (Q) of the inner and outer TENGs for one cycle are shown in Figs. 2b, 2c, and 2d, respectively. Because of the larger functional area, the outer TENG (blue color in Figs. 2b–2d) outperforms the inner TENG (red color in Figs. 2b–2d) in terms of the amplitudes of all electrical outputs. The average and peak power outputs were measured under different resistive loads (Figs. 2e and 2f). The peak power of the outer TENG (red color in Fig. 2f) can reach 18.3 mW at 20 M Ω , which is roughly three times the peak power of inner TENG (7.3 mW) at 40 M Ω (black color in Fig. 2f). The optimal average power of the outer TENG is 1.50 mW at 30 M Ω (red color in Fig. 2e) and 0.52 mW at 60 M Ω (black color in Fig. 2e) for the inner TENG. The average and peak power densities of the AO-TENG considering its volume (0.00074 m³) were 2.73 W/m³ and 34.6 W/m³, respectively.

2.2. Modeling and sea trial of the AO-TENG buoy

The exaggerated swing motion of the AO-TENG buoy benefits its electrical power output. Hence, obtaining the buoy dynamics is crucial

for the energy harvesting system design. However, conducting a field test for our AO-TENG buoy in the Arctic Ocean poses challenges given the remote location, harsh environmental conditions, and significant costs involved. Instead, modeling the Arctic buoy virtually is a cost-effective method for buoy design. A reliable simulation model that demonstrates buoy dynamics under any expected wave conditions helps researchers efficiently optimize the buoy design to achieve greater swing motion amplitude and faster swing motion speed, and consequently guarantee more electrical power output.

To model our Arctic buoy, we first implemented and deployed the original Arctic buoy based on the requirements of a potential user, with all components installed, for a field test in the accessible local wave conditions. By extracting key wave parameters from the time profiles of the collected wave data, we replicated the wave conditions in a simulated environment (using simulation software). The three-dimensional (3D) meshed buoy model, including all mass properties and dynamic parameters was then integrated. Finally, we validated the model by comparing the simulation results with the field test data, focusing on statistical values related to both the wave conditions and the buoy dynamics.

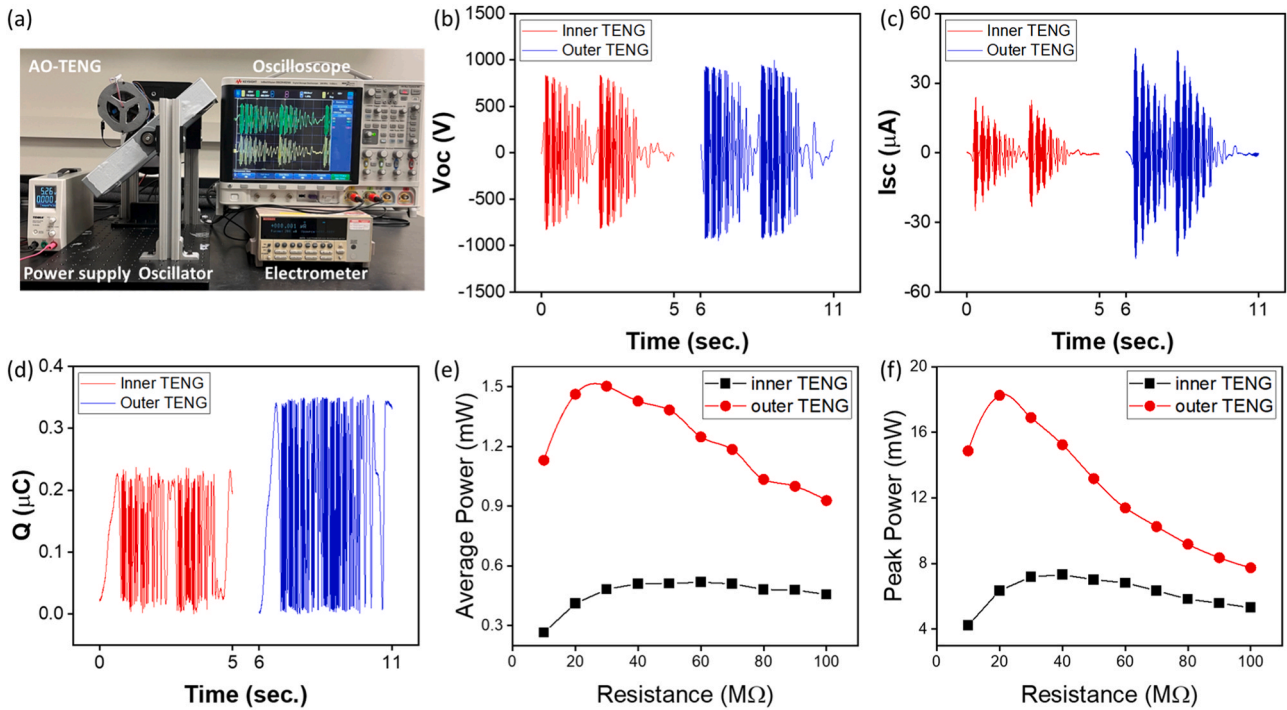


Fig. 2. Output power and current with different resistive loads. (a) The experimental setup of an out-of-water, in-lab, SDOF oscillator with a single AO-TENG. (b) The open-circuit voltage, (c) short-circuit current, and (d) transferred charge of the inner and outer TENGs for one cycle, respectively. (e) Average power and (f) peak power of the inner and outer TENGs.

The AO-TENG buoy was designed to power ocean observation systems, specifically targeting the Upper layer Temperature of the Polar Oceans (UpTempO) buoy [24]. The UpTempO buoy, with a spherical shape and a diameter of 41 cm, has previously been used for critical measurements of ocean temperature and salinity [25,26]. One

requirement in this development of the AO-TENG buoy is to reduce its overall size. This reduction is not only crucial for lowering deployment costs but also holds potential for minimizing the environmental impact of abandoned buoys at the end of their service life in the Arctic Ocean (optimizing internal components count and selecting environmentally

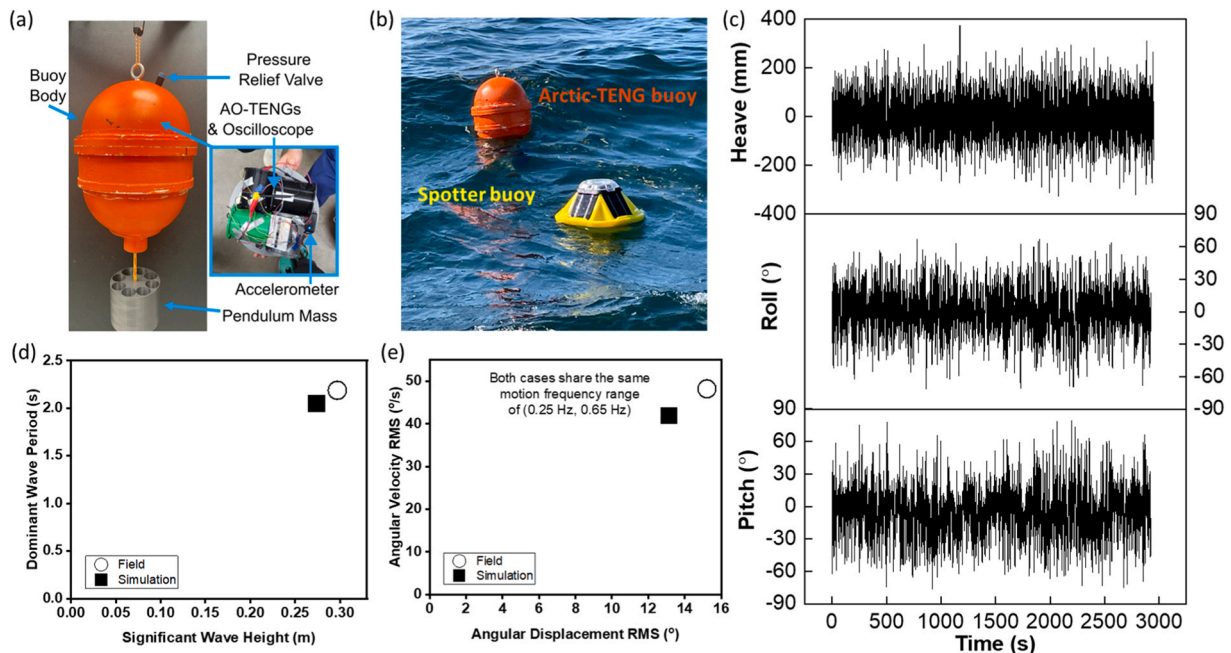


Fig. 3. (a) Schematic of the testing buoy. (b) Photograph of the TENG and Spotter buoys used in the Salish Sea. (c) Time profiles of the heave (wave height) collected by the Spotter buoy (Top graph), and the roll and pitch angular dynamics of the AO-TENG buoy hull recorded by an onboard IMU sensor (Bottom graphs). The heave data were used to extract wave parameters for reconstructing wave conditions in the simulation model, while all collected data (heave, roll, and pitch) served as references to validate the marine dynamic simulation model. Images (d) and (e) show the comparison between field test data and simulation results in wave conditions and the angular velocity of buoy motions, respectively.

friendly materials could be the next steps in this direction). Therefore, the AO-TENG buoy was designed as a smaller size (33 cm in diameter) with a hemispherical bottom dome made from lightweight acrylic material to enhance its stability in the water (Fig. 3a). The middle cylindrical part was added to enlarge the inner space of the buoy for holding the AO-TENG and other electronics. Another hemispherical top dome was used to seal the buoy. A pendulum mass was attached to the bottom of buoy (Fig. 3a) to further increase its swinging motion when facing the waves. The buoy contains an internal platform designed to securely anchor sensors and AO-TENGs. An inertial measurement unit (IMU) sensor logger (3-Space™ Data Logger, YOST LABS) was used to measure the oscillating angle of the buoy in the field test. The IMU sensor was positioned parallel to a pair of AO-TENGs and initialized to differentiate between roll and pitch directions. Additionally, for ease of deployment and retrieval, the buoy is equipped with an eyebolt on the top dome. To mitigate the risk of battery explosion due to potential water leaks, a pressure relief valve (PRV-M10-ASM-R1, BlueRobotics) was installed on top of the buoy. Four AO-TENGs were integrated inside the buoy in two vertical pairs, namely along the roll and pitch directions (Fig. 3a). Therefore, the FMC-TENGs can harvest energy when both buoy's roll and pitch motions happen due to ocean waves. Eight rectifier circuits were used and connected in parallel to collect the power output from the inner and outer TENGs of four AO-TENGs (Fig. S2). A wireless oscilloscope (Pokit Pro, Pokit Innovations) with Bluetooth capability was employed to monitor the electrical output of AO-TENG.

The sea trial took place in the Salish Sea (48.11, -123.02), near the PNNL-Sequim campus. The field trial conducted under natural wave conditions on June 28, 2023, involved using a boat to transport the testing personnel and deploy the AO-TENG buoy. During the test, the AO-TENG buoy was allowed to drift freely for up to 1 hour alongside a Sofar Spotter 3 buoy, which measured ambient wave conditions (Fig. 3b). The two buoys remained within 50 m of each other throughout the test (Fig. 3b). The time profile of wave height was recorded by the Spotter buoy (top graph in Fig. 3c), and time profile of the AO-TENG buoy rotary motions was recorded by the IMU sensor (middle and bottom graphs in Fig. 3c). The natural wave conditions show a significant wave height of 0.30 m and dominant wave period of 2.19 s (symbol with a circle shape in Fig. 3d). In terms of the buoy motion, the root mean square (RMS) of angular displacement and the RMS of angular velocity are 15.22 and 48.25/s, respectively (Fig. 3e). The rotary frequency range is 0.25 Hz–0.65 Hz. Electrical output of the AO-TENGs was recorded (Fig. S3), showing 37 mW of peak power during the sea-trial.

Marine dynamic simulation was performed using *ProteusDS*, a marine dynamic analysis software, to recreate the wave conditions in the Salish Sea and simulate the AO-TENG buoy's motion under these conditions. To replicate the wave environment, we extracted key wave parameters, including significant wave height, dominant wave period, and maximum/minimum wave periods, from the wave surface elevation time profile collected by the Spotter buoy (Table S1). These parameters were used to generate the JONSWAP (Joint North Sea Wave Project) frequency spectrum, which served as the basis for reconstructing the sea trial wave conditions in the simulation [27]. For simplification, the dominant wind and wave directions were not considered. We assumed that the buoy's response would be similar whether it was aligned with or at a 90° angle to the wave direction, and thus, variance due to other offset angles was neglected. Additionally, 3D meshed models of the AO-TENG buoy body, the attached weight, and the intervening rope—each with their specified weights and centers of gravity—were imported into the simulated wave conditions (Fig. S4 and Table S2). Here we assumed that AO-TENGs inside the buoy do not significantly influence the buoy dynamics, considering the light weight (0.2 kg pendulum weight accounts for only 3% of total system mass) and the small swing amplitudes (± 45 -degree maximum amplitude range) and short pendulum arm (0.056 m) of the rotor in AO-TENGs. The detailed discussion of the relative motion is in Note S3 and Table S3. Typically, a sampling range of more than 20–30 times the dominant wave period allows capturing

the full wave spectrum and ensures that the statistical properties of the waves are well represented. The simulation was then conducted over a duration of 350 seconds to balance comprehensive capturing of buoy behavior and optimizing simulation time.

To verify this simulation model, we compared the similarity of the key features obtained from simulation results and field test records. Instead of directly comparing the time profiles, which are random and chaotic, we analyzed data from the simulation and field test to get statistical results. First, the wave conditions were found to be accurately replicated by checking the significant sea height and dominant wave period, which are 0.274 m (7.7% lower) and 2.044 s (6.5% lower) (Fig. 3d). Buoy angular motions also demonstrated similarity. The RMS of angular displacement was 13.148 (13.6% lower), the RMS of angular velocity was 41.857/s (13.2% lower), and the dominant angular motion frequency range (0.25 Hz–0.65 Hz, the same) showed similar values (Fig. 3e). The observed discrepancies in wave conditions may arise from overlooked environmental factors such as wind, currents, incorrect wave direction, or the mean propagation heading. They could also stem from the use of an unsuitable frequency spectrum model, suggesting the need to explore alternatives like the Modified Pierson-Moskowitz spectrum or even custom wave spectra. Additionally, refining the 3D model of the buoy could improve accuracy in predicting buoy dynamics. This includes incorporating detailed geometric features of the floating buoy hull and underwater mass holder instead of relying on simplified geometries, fine-tuning mass properties like the center of gravity and moments of inertia, and accounting for more realistic mechanical properties such as the damping coefficient and rope rigidity. Moreover, using more precise CFD parameters—such as added mass coefficients and drag coefficients for rigid components like the buoy hull and mass holder—would help minimize the difference between simulation results and sea trial observations. In summary, we successfully developed a reliable simulation model.

2.3. Optimization of Arctic-TENG buoy

The verified simulation model of the buoy was employed to predict the angular motions of the buoy under Arctic Ocean conditions and to optimize its design for achieving greater average angular amplitude and angular velocity. This optimization is crucial for maximizing the output power of AO-TENGs. To further estimate the power output of the AO-TENGs in Arctic conditions, we developed a custom desktop buoy motion simulator capable of replicating the buoy roll and pitch motions predicted by the simulation model under Arctic Ocean conditions. The estimated power output of the integrated AO-TENGs was recorded while performing the time profile dynamics.

By applying key wave features, we can accurately replicate Arctic Ocean wave conditions and predict the buoy angular motions using the simulation model. Three years (2013–2015) of standard meteorological data [including significant wave height, dominant wave period (Fig. S5a)], [air temperature and sea surface temperature (Fig. S5b)] during the summer and fall months (July–October) from the National Buoy Center collected in the Arctic Ocean (Station 48214) were used to simulate Arctic Ocean condition in *ProteusDS* [28]. We extracted the most prevalent pair of significant wave height and dominant wave period (1.45 m and 5.7 seconds, respectively) to replicate the most common wave conditions (Fig. 4a). Increasing the range and rate of the buoy swing motion boosts the rotor motion of the AO-TENG, and results in a greater power conversion from wave energy to electricity. Subsequently, we adjusted the length of the intervening rope to identify the best configuration that yields greater resultant angular displacement and angular velocity, ensuring a more considerable harvested power output. The rope length was selected because its adjustment is inexpensive both for buoy dynamic simulation and buoy system fabrication. As in previous analyses, simulations for cases with varying rope lengths were conducted over a duration of 350 seconds, and statistical dynamic behaviors were compared across these different length scenarios. The

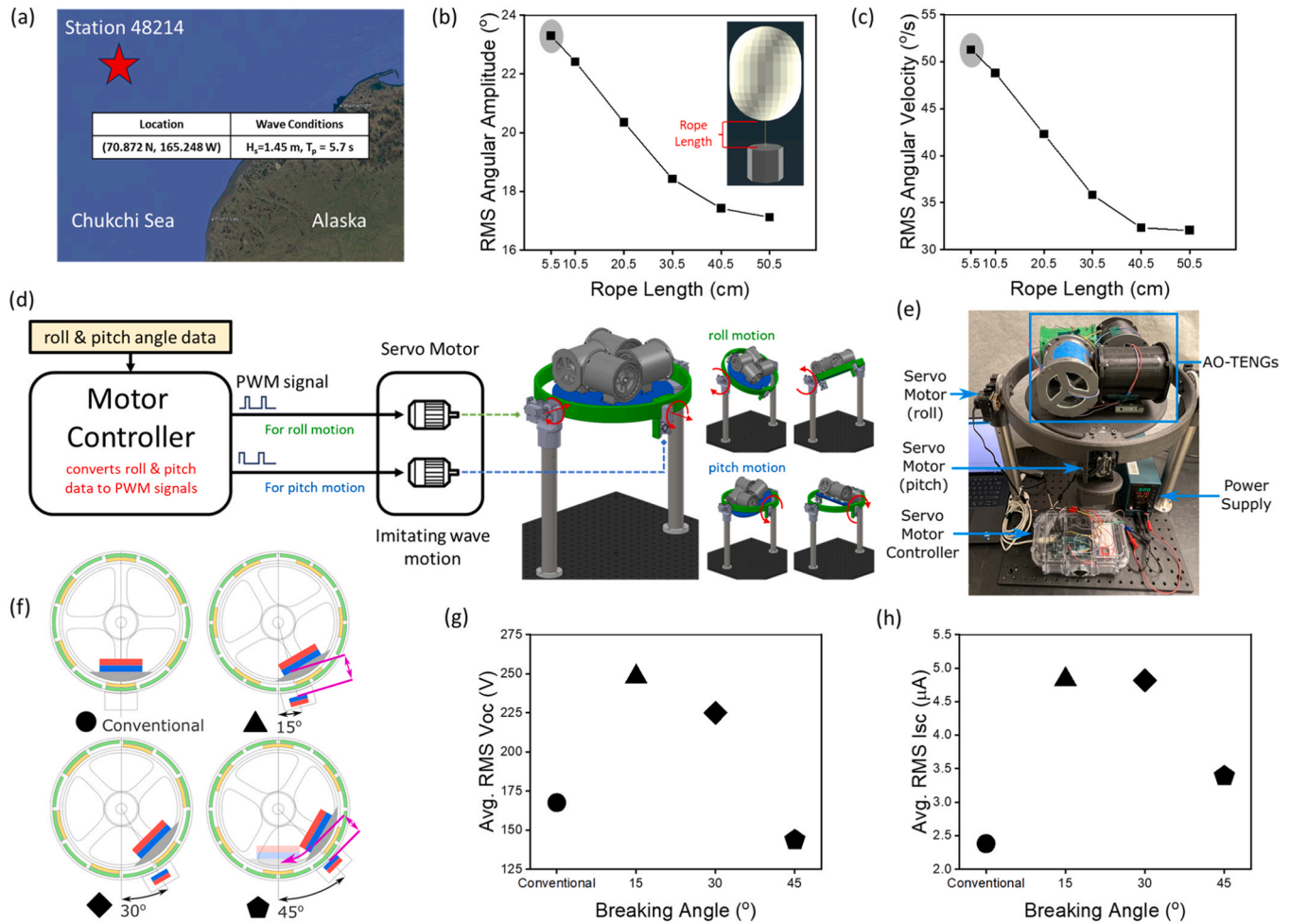


Fig. 4. Optimization of buoy dynamics and AO-TENG performance in the Arctic Ocean. (a) Wave data from the National Buoy Center collected in the Arctic Ocean (Station 48214) near Alaska were used for simulation. Images (b) and (c) depict the simulation results of average angular displacement and angular velocity at various rope lengths, respectively. The shaded area represents a wrongly represented scenario where the pendulum mass collides with the buoy body (Fig. S6). Images (d) and (e) show the design of the buoy motion simulator and the installation method for the AO-TENGs. Image (f) provides schematics of a conventional scenario and selected breaking angles (deciding the rotor begins to rotate from still at tilting angles of 15°, 30°, and 45°) for the AO-TENGs. Adjusting the breaking angle is achieved by changing the distance between two magnets – moving the magnet closer to the one in the rotor increases the breaking angle (Note the varying distances between magnets as indicated in the 15° and 45° breaking angle cases). Graphs (g) and (h) demonstrate the averaged RMS open-circuit voltage and short-circuit current values for four AO-TENGs. In addition, the inserted plots illustrate the open-circuit voltages of AO-TENGs with different breaking angles over time.

average values, angular displacement RMS and angular velocity RMS, were calculated using simulation results (Fig. 4b and c). As depicted in Fig. 4b and c, the shorter rope length corresponds to the greater values for both average angular motions parameters. However, if the rope is too short (5.5 cm, as shown in the shaded case in Fig. 4b and c), pendulum mass colliding with the buoy body cannot be prevented, which is a scenario that the simulation software cannot accurately represent (Fig. S6). Therefore, we still opt for the second shortest rope length of 10.5 cm.

A custom desktop buoy motion simulator was designed for physically reproducing the predicted two-degree-of-freedom (2DOF) motions of the optimized Arctic buoy in the Arctic Ocean, encompassing roll and pitch motions (Fig. 4d). Referring to the coordinate system affixed to the inner plate, which is identical to that used for field tests and simulations, two servo motors were positioned such that their rotational axes were aligned with the X and Y axis, respectively. Only two rotary motions are considered because other motions regarding the remaining degree of freedoms (i.e., surge, sway, and yaw) do not directly contribute to energy harvesting of the C-TENGs. Only the heave motion might be detrimental to rotor swing inside the AO-TENG. Based on the heave data

collected in the field test, acceleration in the heave direction is around 0.99 m/s^2 . Therefore, we ignore the effect of heave motion because of its small acceleration compared to gravitational acceleration. To achieve roll motion, an outer ring (depicted in green in Fig. 4d) was actuated by a servo motor installed to one post and supported by a bearing fixed in the other post on the opposite side. Another motor/bearing pair, responsible for the inner plate (depicted in orange in Fig. 4d) is anchored to the outer ring, providing the pitch motion for the plate.

The servo motors (Sincecam 70 kg High Torque, allowing $\pm 90^\circ$ rotation) of the buoy motion simulator are controlled by a servo motor controller. The servo motor controller converts angle data of the swing motion obtained from buoy modeling results into pulse-width modulation (PWM) signals. This PWM signal directs the servomotors to specific angular positions replicating the roll and pitch motions of the buoy. Four AO-TENGs were integrated into the inner plate of the buoy motion simulator, with their rotational axes aligned with either X or Y axis. The power outputs of four AO-TENGs were connected to eight full-bridge rectifiers to regulate (AC to DC) the electrical output of AO-TENGs (Fig. S2). It is imperative to validate the 2DOF angular motions of the buoy motion simulator. An accelerometer was affixed to the inner plate

of the simulator, aligning the coordinate systems of the accelerometer and the simulator in parallel. Subsequently, we compared the roll and pitch time profiles recorded by the accelerometer with those provided as the input for motors based on the simulation results (Fig. S7a and S7b).

To maximize energy conversion, AO-TENGs, whose configurations require optimization, were integrated into the buoy motion simulator to evaluate their electrical performance under simulated buoy dynamics replicating Arctic Ocean conditions. The breaking angle of the AO-TENG determines the tilting angle at which the rotor begins to swing, impacting power output levels. By adjusting the distance between magnets in the stator and rotor, we selected breaking angles of 15°, 30°, and 45°, while also including a conventional scenario with unrestricted rotor motion (no magnet) for comparison (Fig. 4f). For performance assessment and optimization, the simulator physically replicated the 350-second simulated dynamics data of the buoy with an optimized rope length. In each test cycle, four AO-TENGs were set to identical breaking angles or operated under the conventional condition, and V_{oc} and I_{sc} were measured. For the conventional case, the maximum amplitude of V_{oc} and I_{sc} was relatively lower than any breaking angle conditions (Fig. S8), showing lower RMS I_{sc} than all breaking angle conditions (Fig. 4g) and lower RMS V_{oc} compared to the 15° and 30° breaking angle conditions (Fig. 4h). Large breaking angles (30° and 45°) resulted in fewer opportunities for rotor oscillation, as shown in the time profiles of V_{oc} and I_{sc} (Fig. S7). This led to lower RMS V_{oc} and I_{sc} compared to the smallest breaking angle case (15°) (Figs. 4g and 4h). In summary, the AO-TENG with a breaking angle of a 15° produced the highest electrical output and was selected to predict energy output in the Arctic environment.

To further evaluate the optimal energy output of the AO-TENG in Arctic temperatures, we tested the buoy motion simulator with four AO-TENGs, each with an identical 15° breaking angle, in a chest freezer at -2°C (Fig. 5a). This temperature was selected based on temperature datasets from the same location and period (Fig. S5b), which show the lowest recorded air and sea surface temperatures at -1.75°C and 1.25°C , respectively. The chest freezer environment was preconditioned to -2°C for several hours prior to testing. Given that the main components function well at temperatures as low as -40°C and the low temperature benefits the TENG power generation [15], we anticipate consistent performance and even improved average power output. The buoy motion simulator then operated over a 350-second simulated dynamic cycle, with power output measured across varying resistive loads. The maximum average power output of 2.28 mW was observed at a 20 M Ω load (Fig. 5b), and the instantaneous power output at this optimal load was recorded (Fig. 5c), showing that the majority of peaks range between 10 mW and 20 mW, with the maximum peak power output reaching 22 mW. This power level is sufficient to support more than 1.5

satellite transmissions per day, enabling the transfer of over 500 bytes of data daily. The estimation of energy output of AO-TENG and satellite transmission is detailed in the supplementary material (Note S4, Table S4).

3. Conclusion

We developed an innovative research method that accurately analyzes the impact of actual wave conditions on the TENG's energy harvesting behavior. A sea trial was conducted in nearshore waters leading to the Pacific Ocean to gather empirical data on sea states, buoy motion, and the electrical output of the AO-TENG. The trial recorded a significant wave height of 0.30 m and a dominant wave period of 2.19 s. Buoy motion, characterized by RMS angular displacement (15.22°) and angular velocity ($48.25^{\circ}/\text{s}$), was measured. Under these conditions, the AO-TENG demonstrated a peak power output of 37 mW. The sea state and buoy motion data were then used to validate the simulation model. Validation results show that the wave conditions in the simulation replicated a significant sea height (0.27 m) and a dominant wave period (2.04 s), with 10 % and 6.8 % differences compared to the sea-trial data. Buoy angular motions, RMS angular displacement (13.15°), and angular velocity ($41.86^{\circ}/\text{s}$) show 13.6 % and 13.2 % differences, showing fair agreement with sea-trial data.

For improved future accuracy, alternative frequency spectrum models could be applied to enhance wave condition reconstruction, along with incorporating comprehensive environmental factors like wind and mean propagation heading. Additionally, refining the buoy's 3D model and adjusting its mass properties, applying more realistic mechanical properties, and incorporating more accurate CFD parameters could further optimize the alignment between simulated and sea trial performance. Furthermore, a greater number of comparisons between experimental and simulation results is part of our future work. Sea trials under varied conditions—such as revisiting the same location (e.g., Salish Sea) during different seasons, exploring various locations during the same period, or conducting trials across distinct locations and times—would provide valuable insights into the model's performance. These trials could help refine our understanding, assess the model's reliability, and identify any required adaptations to improve its versatility across different scenarios.

The verified simulation model of the buoy was employed to predict its angular motions under Arctic Ocean conditions and to optimize buoy design for achieving greater average angular amplitude and velocity, thereby maximizing the output power of the AO-TENG. The numerically optimized buoy dynamics, as determined by the simulation model, were experimentally replicated using a custom buoy motion simulator. The AO-TENGs were then tested under these simulated conditions to

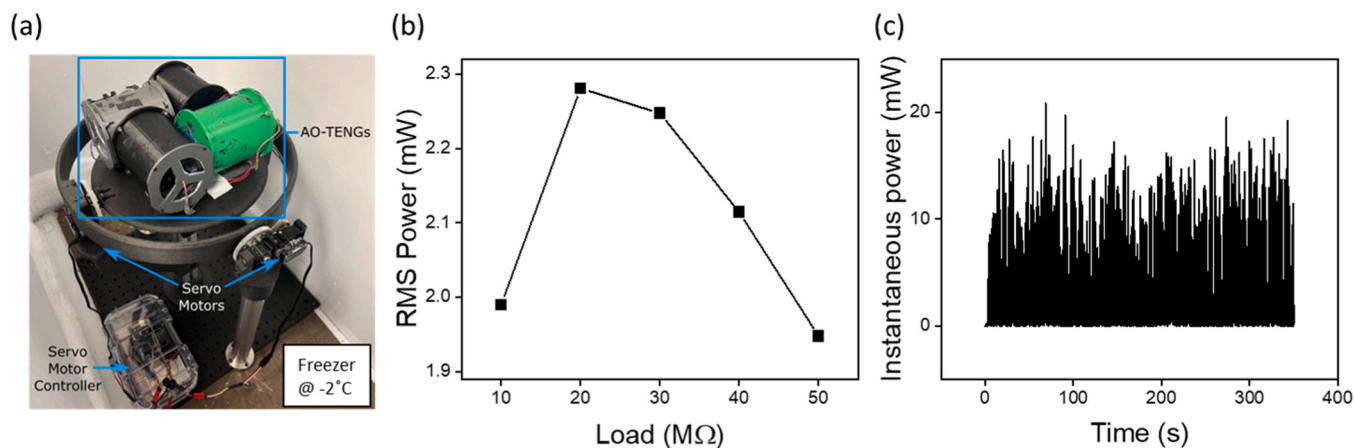


Fig. 5. Prediction of Electrical Power Output in the Arctic Ocean. (a) Buoy motion simulator integrated with four AO-TENGs stored in a refrigerator at -2°C . (b) RMS power of AO-TENGs with different resistive loads. (c) Instantaneous power output of AO-TENGs at the optimum load (20 M Ω).

evaluate its performance in Arctic Ocean conditions. This power level is sufficient to support more than 1.5 satellite transmissions per day, enabling the transfer of over 500 bytes of data daily. These results highlight the AO-TENG's potential to provide reliable power for ocean buoys in the Arctic Ocean. Future experimental efforts will aim to validate these predictions through in-field deployments, focusing on their ability to sustain and support electronic operations in Arctic conditions.

Given the harsh working conditions of the Arctic Ocean, a long-term durability test of the fully integrated energy harvesting device should be prioritized in future work to ensure the AO-TENG operates reliably in low temperatures. This includes verifying the buoy hull's ability to withstand potential impacts, preventing structural damage, and ensuring watertight integrity throughout the operational period. Finally, it is also worth noting the potential alternative applications of our AO-TENG beyond energy harvesting, such as an sensor for measuring wave parameters in the Arctic Ocean [29].

4. Experimental method

4.1. Fabrication of the Arctic-TENG buoy

The bulk of FMC-TENG's components were manufactured from PLA using a 3D printer (Prusa MK4). These components include the rotor, stator, rotor end caps, stator endcaps, and magnet/weight/desiccant holder. The rotor and stator each has pads for the FEP and aluminum, respectively. The gap between the rotor and stator determines the distance between the aluminum and FEP, and therefore is a very important metric for the TENG. The outer diameter of the rotor was 85.6 mm, and the inner diameter of the stator was 87 mm. The thicknesses of the FEP and aluminum (including adhesive thickness) were each about 0.09 mm, which means that the aluminum and FEP were separated by 1.22 mm. The area of each pad (FEP or aluminum) was 457 mm²; therefore, the total area of aluminum was twice the area of FEP. To improve surface charge density, three strips of rabbit fur were distributed equally around the stator and glued between aluminum pads. A magnet was set in a slot in the stator and tungsten powder mixed with epoxy was put into the slot in the rotor. O-rings were also used between the stator and its end caps. A bearing was affixed to each rotor end cap, and a shaft attached to each stator end cap went through both bearings, allowing the rotor to spin independently of the stator.

The buoy consists of two acrylic hemispheres, a central cylinder, and a housing platform. The acrylic hemispheres were manufactured by Hicaptain. The central cylinder was made from PLA using a 3D printer (Creality Cr-10 Max). One acrylic hemisphere was glued to one side of the cylinder, but to allow easy access to the inside of the buoy, the other one was not glued. To better seal the buoy and prevent water leaks, an O-ring was installed in a slot on the side of the central cylinder and grease was added when closing and tightening the other acrylic hemisphere with eight pairs of bolts and nuts. Desiccant was used not only for moisture control but also to add necessary weight for adjusting the buoy's center of gravity.

4.2. Characterizations and measurements

The AO-TENG was tested using an out-of-water, SDOF oscillator (Fig. 2a), consisting of a two-bar arm linkage connected to a DC motor that oscillated the testing platform in a controlled rocking motion. The oscillator replicated 0.2 m high waves for all tests, with the wave frequency set at 0.2 Hz. To capture the electrical output of the AO-TENG, an oscilloscope (Agilent Technologies, MSO-X 3034 A) and a high-voltage probe (Cal Test Electronics, GE3225) with a high internal impedance (100 M Ω) were used. Additionally, short-circuit current measurements were taken using an electrometer (Keithley 6517 A). Low-temperature energy harvesting predictions were conducted within a chest freezer (LABRepCo, LABL-15-CT40) to simulate Arctic-like

conditions and assess the performance of the AO-TENG under extreme environments. During the field test in the Salish Sea, buoy dynamics and power output were measured. A Yoti-3 space sensor (IMU sensor) was used to measure the oscillating angle of the buoy. This IMU sensor was placed inside the buoy, positioned parallel to a pair of AO-TENGs, and initialized to differentiate between roll and pitch directions. A wireless oscilloscope (Pokit Pro, Pokit Innovations) with Bluetooth capability was employed to monitor the output power.

CRedit authorship contribution statement

Zhaocheng Lu: Writing – original draft, Visualization, Methodology, Investigation, Formal analysis, Data curation. **Wonseop Hwang:** Writing – original draft, Investigation, Formal analysis, Data curation. **Hyunjun Jung:** Writing – original draft, Methodology, Investigation, Formal analysis, Data curation, Conceptualization. **Zhiqun Daniel Deng:** Writing – review & editing, Supervision, Resources, Methodology, Conceptualization. **Andrea Copping:** Writing – review & editing, Supervision, Project administration, Investigation. **Ruth Branch:** Writing – review & editing, Validation, Investigation. **Brianna Friedman:** Writing – review & editing, Validation, Investigation.

Declaration of Competing Interest

The authors declare the following financial interests/personal relationships which may be considered as potential competing interests: Zhiqun Daniel Deng reports financial support was provided by US Department of Energy Water Power Technologies Office. If there are other authors, they declare that they have no known competing financial interests or personal relationships that could have appeared to influence the work reported in this paper.

Acknowledgements

This research was funded by the U.S. Department of Energy (DOE) Water Power Technologies Office. The study was conducted by the Pacific Northwest National Laboratory (PNNL), which is operated by Battelle for the DOE under Contract DE-AC05-76RL01830. The authors would like to thank the crew of the PNNL R/V Strait Science for their assistance during the field test.

Appendix A. Supporting information

Supplementary data associated with this article can be found in the online version at [doi:10.1016/j.nanoen.2024.110641](https://doi.org/10.1016/j.nanoen.2024.110641).

Data Availability

Data will be made available on request.

References

- [1] V.M. Kattsov, V.E. Ryabinin, J.E. Overland, M.C. Serreze, M. Visbeck, J.E. Walsh, W. Meier, X. Zhang, Arctic sea-ice change: a grand challenge of climate science, *J. Glaciol.* 56 (2010) 1115–1121, <https://doi.org/10.3189/002214311796406176>.
- [2] J. Overland, E. Dunlea, J.E. Box, R. Corell, M. Forsius, V. Kattsov, M.S. Olsen, J. Pawlak, L.-O. Reiersen, M. Wang, The urgency of Arctic change, *Polar Sci.* 21 (2019) 6–13, <https://doi.org/10.1016/j.polar.2018.11.008>.
- [3] M. Lin, C. Yang, Ocean observation technologies: a review, *Chin. J. Mech. Eng.* 33 (2020) 32, <https://doi.org/10.1186/s10033-020-00449-z>.
- [4] Arctic Buoys Help Tell Story of Planetary Climate Change, Wild Rose Education (2023). (<https://www.wildroseeducation.com/post/arctic-buoys-help-tell-story-of-climate-change>) (accessed April 27, 2023).
- [5] Photo story: So how do you maintain a huge weather buoy network?, (n.d.). (<https://www.noaa.gov/multimedia/photos-images/photo-story-so-how-do-you-main-tain-huge-weather-buoy-network>) (accessed May 12, 2023).
- [6] R. Branch, F. Ticona Rollano, E. Cotter, J.R. McVey, R.J. Cavagnaro, I. Rigor, Marine renewable energy for Arctic observations, *Front. Mar. Sci.* 9 (2022). (<https://www.frontiersin.org/articles/10.3389/fmars.2022.970337>) (accessed January 25, 2023).

- [7] M. Xu, T. Zhao, C. Wang, S.L. Zhang, Z. Li, X. Pan, Z.L. Wang, High power density tower-like triboelectric nanogenerator for harvesting arbitrary directional water wave energy, *ACS Nano* 13 (2019) 1932–1939, <https://doi.org/10.1021/acsnano.8b08274>.
- [8] FEP and PTFE Fluoropolymers: Eco-friendly and FDA-Approved Materials for a Sustainable Future, (n.d.). (<https://fluoron.com/blog/fep-and-ptfe-fluoropolymer-s-eco-friendly-and-fda-approved-materials-for-a-sustainable-future/>) (accessed December 10, 2024).
- [9] Z.L. Wang, T. Jiang, L. Xu, Toward the blue energy dream by triboelectric nanogenerator networks, *Nano Energy* 39 (2017) 9–23, <https://doi.org/10.1016/j.nanoen.2017.06.035>.
- [10] Z.L. Wang, Catch wave power in floating nets, *Nature* 542 (2017) 159–160, <https://doi.org/10.1038/542159a>.
- [11] C. Rodrigues, M. Ramos, R. Esteves, J. Correia, D. Clemente, F. Gonçalves, N. Mathias, M. Gomes, J. Silva, C. Duarte, T. Morais, P. Rosa-Santos, F. Taveira-Pinto, A. Pereira, J. Ventura, Integrated study of triboelectric nanogenerator for ocean wave energy harvesting: performance assessment in realistic sea conditions, *Nano Energy* 84 (2021) 105890, <https://doi.org/10.1016/j.nanoen.2021.105890>.
- [12] X. Wang, L. Chen, Z. Xu, P. Chen, C. Ye, B. Chen, T. Jiang, Z. Hong, Z.L. Wang, High-durability stacked disc-type rolling triboelectric nanogenerators for environmental monitoring around charging buoys of unmanned ships, *Small* 20 (2024) 2310809, <https://doi.org/10.1002/smll.202310809>.
- [13] C. Zhang, S. Yang, X. Dai, Y. Tu, Z. Du, X. Wu, Y. Huang, J. Fan, Z. Hong, T. Jiang, Z.L. Wang, Hybridized triboelectric-electromagnetic nanogenerators for efficient harvesting of wave energy for self-powered ocean buoy, *Nano Energy* 128 (2024) 109929, <https://doi.org/10.1016/j.nanoen.2024.109929>.
- [14] C.X. Lu, C.B. Han, G.Q. Gu, J. Chen, Z.W. Yang, T. Jiang, C. He, Z.L. Wang, Temperature effect on performance of triboelectric nanogenerator, *Adv. Eng. Mater.* 19 (2017) 1700275, <https://doi.org/10.1002/adem.201700275>.
- [15] M.-L. Seol, J.-W. Han, D.-I. Moon, M. Meyyappan, Triboelectric nanogenerator for Mars environment, *Nano Energy* 39 (2017) 238–244, <https://doi.org/10.1016/j.nanoen.2017.07.004>.
- [16] X. Wen, Y. Su, Y. Yang, H. Zhang, Z.L. Wang, Applicability of triboelectric generator over a wide range of temperature, *Nano Energy* 4 (2014) 150–156, <https://doi.org/10.1016/j.nanoen.2014.01.001>.
- [17] H. Jung, H. Ouro-Koura, A. Salalila, M. Salalila, Z.D. Deng, Frequency-multiplied cylindrical triboelectric nanogenerator for harvesting low frequency wave energy to power ocean observation system, *Nano Energy* 99 (2022) 107365, <https://doi.org/10.1016/j.nanoen.2022.107365>.
- [18] H. Jung, B. Friedman, W. Hwang, A. Copping, R. Branch, Z.D. Deng, Self-powered arctic satellite communication system by harvesting wave energy using a triboelectric nanogenerator, *Nano Energy* 114 (2023) 108633, <https://doi.org/10.1016/j.nanoen.2023.108633>.
- [19] B. Zhao, Z. Li, X. Liao, L. Qiao, Y. Li, S. Dong, Z. Zhang, B. Zhang, A heaving point absorber-based ocean wave energy convertor hybridizing a multilayered soft-brush cylindrical triboelectric generator and an electromagnetic generator, *Nano Energy* 89 (2021) 106381, <https://doi.org/10.1016/j.nanoen.2021.106381>.
- [20] C. Han, Z. Cao, Z. Yuan, Z. Zhang, X. Huo, L. Zhang, Z. Wu, Z.L. Wang, Hybrid triboelectric-electromagnetic nanogenerator with a double-sided fluff and double halfbach array for wave energy harvesting, *Adv. Funct. Mater.* 32 (2022) 2205011, <https://doi.org/10.1002/adfm.202205011>.
- [21] Z. Yang, J. Shen, X. Qu, Z. Lai, L. Ji, J. Cheng, Charge pumping triboelectric nanogenerator with dust clearance and elastic support for wind energy harvesting, *Nano Energy* 131 (2024) 110263, <https://doi.org/10.1016/j.nanoen.2024.110263>.
- [22] W. Liu, X. Wang, Y. Wang, H. Xu, Y. Nan, J. Niu, J. Xiong, H. Yang, T. Liu, L. Yang, Enhancing the output performance of triboelectric nanogenerator based on soft-contact coaxial double-rotation structure, *Adv. Sustain. Syst.* 8 (2024) 2300430, <https://doi.org/10.1002/advsu.202300430>.
- [23] I. Gonçalves, C. Rodrigues, J. Ventura, Sea state adaptation enhances power output of triboelectric nanogenerators for tailored ocean wave energy harvesting, *Adv. Energy Mater.* 14 (2024) 2302627, <https://doi.org/10.1002/aenm.202302627>.
- [24] UpTempO - Home, (n.d.). (<https://psc.apl.washington.edu/UpTempO/>) (accessed November 1, 2024).
- [25] V. Hill, B. Light, M. Steele, A.L. Sybrandy, Contrasting sea-ice algae blooms in a changing arctic documented by autonomous drifting buoys, *J. Geophys. Res.: Oceans* 127 (2022), <https://doi.org/10.1029/2021JC017848>.
- [26] V.J. Hill, B. Light, M. Steele, R.C. Zimmerman, Light availability and phytoplankton growth beneath arctic sea ice: integrating observations and modeling, *J. Geophys. Res.: Oceans* 123 (2018) 3651–3667, <https://doi.org/10.1029/2017JC013617>.
- [27] K. Hasselmann, T.P. Barnett, E. Bouws, H. Carlson, D.E. Cartwright, K. Enke, J. Ewing, A. Gienapp, D. Hasselmann, P. Kruseman, others, Measurements of wind-wave growth and swell decay during the Joint North Sea Wave Project (JONSWAP), *Ergaenzungsheft Zur. Dtsch. Hydrogr. Z., Reihe A* (1973).
- [28] National data buoy center, Station 48214 - Klondike (MOB1), (n.d.). (https://www.ndbc.noaa.gov/station_page.php?station=48214) (accessed February 1, 2024).
- [29] Y. Peng, H. Liu, H. Guo, Y. Gong, F. Shen, Q. Zhang, Z. Li, Toward highly sensitive ocean-wave monitoring with sliding-triboelectric effect: modeling, experimental validation, and demonstration, *IEEE/ASME Trans. Mechatron.* (2024) 1–10, <https://doi.org/10.1109/TMECH.2024.3382368>.